Front. Earth Sci. 2023, 17(2): 407–416
https://doi.org/10.1007/s11707-022-1003-4

RESEARCH ARTICLE

Physical processes associated with movement of maximum wind of Typhoon Rammasun (2014)

Xin QUAN, Xiaofan LI (✉), Guoqing ZHAI

Key Laboratory of Geoscience Big Data and Deep Resource of Zhejiang Province, School of Earth Sciences, Zhejiang University, Hangzhou 310027, China

Abstract In this study, the movement of the maximum wind of Typhoon Rammasun (2014) was measured by the radial movement of the maximum symmetric rotational kinetic energy. The weather research and forecasting (WRF) model was used to simulate Typhoon Rammasun, and validated simulation data for the lower troposphere were analyzed to examine the physical processes responsible for the radial movement of the maximum wind. The radii, where maximum symmetric rotational kinetic energy and its maximum tendency were located, were compared to explain radial movement. The tendency in the lower troposphere is controlled by the flux convergence of symmetric rotational kinetic energy and the conversion from symmetric divergent kinetic energy to symmetric rotational kinetic energy, as well as frictional dissipation in the symmetric rotational kinetic energy budget. The inward movement before rapid intensification (RI) resulted from radial flux convergence; cyclonic circulation develops while moving inward. Stationary maximum symmetric rotational kinetic energy and RI were caused by the conversion, which was observed to be proportional to the symmetric rotational kinetic energy. Landfall increased terrain-induced friction dissipation, which led to outward movement and ended the RI.

Keywords typhoon, radial movement of maximum wind, symmetric rotational kinetic energy, rapid intensification, kinetic energy budget, flux convergence, conversion

1 Introduction

Tropical cyclones characterized by strong winds and heavy precipitation often result in tremendous loss of life and property, especially when they make landfall. Both the strong winds and heavy precipitation occur inside the eyewall of the cyclone, where strong upward motions associated with convergence in the lower troposphere and divergence in the upper troposphere produce heavy convective rainfall. Since the maximum winds occur inside the eyewalls, the radius of the maximum wind is often similar to that of the eyewall. The variations in these radii also being similar, the variations in the radius of the eyewall can be examined by analyzing the variations in the radius of the maximum wind (e.g., Willoughby et al., 1982). In their idealized numerical simulation, Stern et al. (2015) showed that contraction of the radius of maximum wind and intensification of tropical cyclones begin simultaneously, but the contraction is halted long before the tropical cyclone reaches its maximum intensity. They found that the halting of the contraction results from the rapid increase in sharpness of the tangential wind near the eyewall. Qin et al. (2016) analyzed the eyewall sizes of rapidly intensifying hurricanes using the extended best-track data set for 1990–2014 to reveal that over half of them had steady eyewall sizes. They also observed that eyewall sizes appeared steady more frequently for sizes less than 50 km. Qin and Wu (2021) showed that synoptic scale circulations may have played an important role in the expansion of the eyewall during the rapid intensification (RI) of Hurricane Helene (2006).

Various methods have been proposed to quantitatively analyze the radial movement of the maximum wind in tropical cyclones. Willoughby et al. (1982) derived an equation where the change in the radius of the maximum wind of a tropical cyclone is expressed as the difference between the intensification rate of the cyclone and the local tangential wind tendency at the radius of arrival of the maximum wind, divided by the radial gradient of the tangential wind. Kieu (2012) constructed a dynamic equation from the momentum budget of tangential winds, which includes the inward advection by the radial inflow

Received December 25, 2021; accepted May 19, 2022

E-mail: xiaofanli@zju.edu

and frictional dissipation. He discovered that the inward advection by the radial inflow is more important during the early development of hurricanes, and frictional dissipation becomes significant when hurricanes are strong enough. Stern et al. (2015) constructed a diagnostic equation for the contraction rate of the radius of maximum wind, where the contraction rate is expressed as the radial gradient of the local tendency of the azimuthally averaged tangential wind divided by the curvature of the azimuthally averaged tangential wind in the radial direction at the radius of maximum wind. The methods proposed by Kieu (2012) and Stern et al. (2015) yield different conclusions. Li et al. (2019) undertook a comparison of these two methods and observed that the method proposed by Kieu (2012) is a special case of the method proposed by Willoughby et al. (1982) while Stern et al.'s method can be extended to generate the tendency of the radius of the maximum wind of tropical cyclones. Li et al. (2021) further showed that the budgets of both the tangential wind and the change rate in the radius of maximum wind can be used to explain the dynamics associated with the relationship between RI and rapid contraction of the radius of maximum wind. They observed that the moderate negative radial gradient of the radial vorticity flux and the small curvature of the radial distribution of tangential wind near the radius corresponding to maximum wind are physical processes that favor the rapid contraction of the radius of maximum wind.

In this study, the physical processes responsible for the movement of the maximum wind of a tropical cyclone were investigated from the point of view of kinetic energy budgets. The Super Typhoon Rammasum that occurred in 2014 was simulated using the Weather Research and Forecasting (WRF) model. The movements of the maximum wind before, during, and after RI of Rammasun were identified as corresponding to the decreased, barely changed, and increased radial distances of the maximum symmetric rotational kinetic energy in the cylindrical coordinate system. The radial distances, where the maximum symmetric rotational kinetic energy and the maximum tendency of the symmetric rotational kinetic energy were located, were compared, and the budget of the symmetric rotational kinetic energy was analyzed to examine the physical processes that account for the radial movement of the maximum wind of the tropical cyclone.

In the next section, an overview of Super Typhoon Rammasun (2014), the model configuration, and the physical package are introduced. The results are presented and discussed in Section 3. A summary is provided in Section 4.

2 Overview of Typhoon Rammasun and model setup

Typhoon Rammasun formed in the northwest Pacific Ocean at 06:00 UTC on July 12, 2014, and it then strengthened to a severe typhoon while it moved westward. Rammasun made its first landfall on southern Luzon Island of the Philippines at 09:00 UTC on July 15. While it continued to move northwestward, Rammasun started to strengthen rapidly at 06:00 UTC on July 17 and became a super typhoon at 02:00 UTC on July 18. Rammasun made the second landfall in Wenchang, Hainan, China, 4 h later. With a minimum central pressure of 918 hPa and a maximum wind speed of 72 $m \cdot s^{-1}$, Rammasun is the strongest among the typhoons that have made landfall along the coast of China since 1973.

Typhoon Rammasun was simulated using the WRF model (version 4.0; available at WRF website) (Skamarock et al., 2019). The initial and lateral atmospheric boundary conditions were obtained from Global Forecast System analysis data (available at NOAA website) (Kalnay et al., 1996) having a horizontal resolution of 0.5° × 0.5°. The model uses two-way nesting and three nested domains. The model configuration and physical schemes are listed in Table 1. The simulations were compared with observations in terms of the minimum central pressure and maximum wind (Fig.1). The observations used in this study were obtained from the Joint Typhoon Warning Center (JTWC) best-track data (available at METOC website). A comparison between the simulations and observations showed that the model reproduced Typhoon Rammasun with reasonable accuracy. Therefore, the simulation data can be used to analyze the physical processes responsible for the movement of the maximum wind of Rammasun.

3 Results

In this study, the winds were first separated into environmental and typhoon winds using both the Kurihara's filtering method (Kurihara et al., 1993, 1995) and multiscale window transform (Liang and Anderson, 2007) because the combination of these two methods achieves better separation than they do individually (Zhao et al. 2015). The detailed separation procedure can be found in Zhao et al. (2015). Typhoon winds were further separated into rotational winds and divergent winds. Divergence is first calculated from the typhoon wind; the iterative method (Li et al. 2012) considering zero winds along lateral boundaries is then used to calculate the velocity potential from which divergent wind is finally calculated. Since the typhoon wind is the sum of divergent and rotational winds, rotational wind is determined by subtracting the divergent wind from the typhoon wind. The maximum winds of typhoons are mainly rotational, while clouds and precipitation result from secondary circulations with inward radial flows in the lower troposphere and outward radial flows in the upper troposphere. To analyze the evolution of the maximum winds of a typhoon, a cylindrical coordinate

Table 1 (a) Model configuration and (b) physics schemes.

(a)

Domain	01	02	03
Grid pints	299 × 235	634 × 538	1015 × 904
Horizontal grid spacing /km	18	6	2
Vertical level	50	50	50
Model top/hPa	10	10	10
Cumulus scheme	Used	Not used	Not used

(b)

Model physics	Scheme
Microphysics	WSM6 (Hong and Lim, 2006)
Planetary boundary layer	BouLac (Bougeault and Lacarrere, 1989)
Cumulus scheme	Kain-Fritsch (Kain, 2004)
IR radiative scheme	(Mlawer et al., 1997)
Solar radiative scheme	(Dudhia, 1989)
Surface layer	Monin-Obukhov (Moon et al., 2007)
Land surface	Noah (Ek et al., 2003)
Integration time period	06:00 UTC on July 16 – 06:00 UTC on July 19

system with the center moving with the typhoon center was established, and both rotational and divergent winds were separated into symmetric and asymmetric components. In this dynamic framework, the maximum winds of a typhoon are represented by their symmetric rotational winds, which can be measured by symmetric rotational kinetic energy. In this study, the symmetric rotational kinetic energy ($K_{\psi s}$) is defined as

$$K_{\psi s} = \frac{\boldsymbol{V}_{\psi s}{}^2}{2}, \tag{1}$$

where $\boldsymbol{V}_{\psi s}$ is the symmetric rotational wind vector.

Figure 2 shows the variation over time in the radial distance of the maximum symmetric rotational kinetic energy of the simulated Typhoon Rammasun from the typhoon center. The radial distance decreased from 70 km to approximately 30 km nearly linearly during the period of 06:00 UTC on July 16 – 13:00 UTC on July 17. It then remained approximately 30 km from 13:00 UTC on July 17 to 08:00 UTC on July 18. The radial distance increased from 30 km to 36 km from 09:00 UTC on July 18 to 15:00 UTC on July 18. It prevailed at 36 km after 16:00 UTC on July 18. Figures 1 and 2 reveal that Rammasun strengthened gradually as the radial distance decreased from 70 km to 30 km, and intensified rapidly when the radial distance prevailed approximately 30 km, and weakened as the radial distance increased from 30 km to 36 km making landfall in Hainan, China. Since the maximum winds of typhoons usually occur in the lower troposphere, the 900-hPa simulation data for 00:00 UTC on July 17, 17:00 UTC on July 17 and 12:00 UTC on July 18, 2014 were used to analyze the dominant physical processes responsible for inward radial movement, stationary condition and outward movement of maximum symmetric rotational kinetic energy, respectively.

To understand the physical processes responsible for the radial movement of the maximum symmetric rotational kinetic energy, the symmetric rotational kinetic energy budget was analyzed. The symmetric rotational kinetic energy budget can be expressed as

$$\begin{aligned} DK_{\psi s} = &\left(K_e, K_{\psi s}\right) + \left(K_{\psi a}, K_{\psi s}\right) + \left(K_{\chi s}, K_{\psi s}\right) + \left(K_{\chi a}, K_{\psi s}\right) \\ &+ FK_{\psi s} + D_{\psi s} + R_{\psi s}, \end{aligned} \tag{2}$$

where

$$\left(K_e, K_{\psi s}\right) = - < \boldsymbol{V}_{\psi s} \cdot (\boldsymbol{V} \cdot \nabla)\boldsymbol{V}_e > - < \omega \frac{\partial}{\partial p}\boldsymbol{V}_e \cdot \boldsymbol{V}_{\psi s} > - < f(\boldsymbol{k} \times \boldsymbol{V}_e) \cdot \boldsymbol{V}_{\psi s} >, \tag{2a}$$

$$\left(K_{\psi a}, K_{\psi s}\right) = - < \boldsymbol{V}_{\psi s} \cdot (\boldsymbol{V} \cdot \nabla)\boldsymbol{V}_{\psi a} > - < \omega \frac{\partial}{\partial p}\boldsymbol{V}_{\psi a} \cdot \boldsymbol{V}_{\psi s} > - < f\left(\boldsymbol{k} \times \boldsymbol{V}_{\psi a}\right) \cdot \boldsymbol{V}_{\psi s} >, \tag{2b}$$

$$\left(K_{\chi s}, K_{\psi s}\right) = - < \boldsymbol{V}_{\psi s} \cdot (\boldsymbol{V} \cdot \nabla)\boldsymbol{V}_{\chi s} > - < \omega \frac{\partial}{\partial p}\boldsymbol{V}_{\chi s} \cdot \boldsymbol{V}_{\psi s} > - < f\left(\boldsymbol{k} \times \boldsymbol{V}_{\chi s}\right) \cdot \boldsymbol{V}_{\psi s} >, \tag{2c}$$

$$\left(K_{\chi a}, K_{\psi s}\right) = - < \boldsymbol{V}_{\psi s} \cdot (\boldsymbol{V} \cdot \nabla)\boldsymbol{V}_{\chi a} > - < \omega \frac{\partial}{\partial p}\boldsymbol{V}_{\chi a} \cdot \boldsymbol{V}_{\psi s} > - < f\left(\boldsymbol{k} \times \boldsymbol{V}_{\chi a}\right) \cdot \boldsymbol{V}_{\psi s} >, \tag{2d}$$

$$FK_{\psi s} = - < \nabla \cdot \left(\boldsymbol{V} \cdot \frac{\boldsymbol{V}_{\psi s}{}^2}{2}\right) > - < \frac{\partial}{\partial p}\left(\omega \frac{\boldsymbol{V}_{\psi s}{}^2}{2}\right) > - < \nabla \cdot \left(\boldsymbol{V}_{\psi s} \varnothing\right) >, \tag{2e}$$

$$D_{\psi s} = \boldsymbol{V}_{\psi s} \cdot \boldsymbol{F}, \tag{2f}$$

$$R_{\psi s} = - < \boldsymbol{V}_{\psi s} \cdot \frac{\partial}{\partial t}\boldsymbol{V}_e > - < \boldsymbol{V}_{\psi s} \cdot \frac{\partial}{\partial t}\boldsymbol{V}_{\chi s} >, \tag{2g}$$

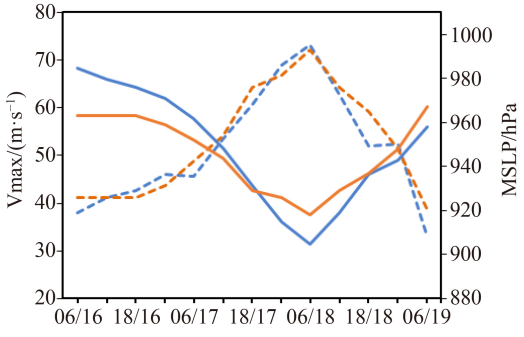

Fig. 1 Maximum wind speeds (solid lines, m·s^{-1}) and maximum sea level pressures (dashed lines, hPa). Time is UTC.

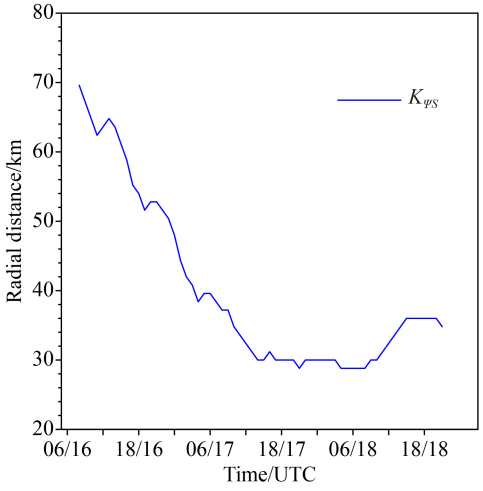

Fig. 2 Time series of radial distance (km) of maximum symmetric rotational kinetic energy from typhoon center.

$$< >= \frac{\int_0^{2\pi} () \mathrm{d}\theta}{2\pi}. \tag{2h}$$

The definitions and physical meanings of the symbols in Eq. (2) are shown in Table 2. In this study, the time step of the model is 1 min. As an example, in addition to the output at hour 1 (minute 60), the model also has wind outputs at minutes 59 and 61. $DK_{\psi s}$ was calculated by determining the difference in $K_{\psi s}$ between minutes 61 and 59 and dividing by 2. $R_{\psi s}$ was also calculated in a similar manner (Eq. (2g)). $D_{\psi s}$ Eq. (2f) was calculated as the difference between $DK_{\psi s}$ and $[(K_e, K_{\psi s}) + (K_{\psi a}, K_{\psi s}) + (K_{\chi s}, K_{\psi s}) + (K_{\chi a}, K_{\psi s}) + FK_{\psi s} + R_{\psi s}]$. Thus, an accurate calculation of the symmetric rotational kinetic energy is guaranteed.

At 00:00 UTC on July 17, the radius of maximum positive tendency of the maximum symmetric rotational kinetic energy is smaller than the radius of maximum symmetric rotational kinetic energy $[DK_{\psi s} > 0]$, which is indicative of the inward radial movement of the maximum symmetric rotational kinetic energy (Fig. 3(a)). Although the magnitude of the conversion from symmetric divergent kinetic energy to symmetric rotational kinetic energy $\left[(K_{\chi s}, K_{\psi s}) > 0\right]$ was larger than that of the flux convergence $\left[FK_{\psi s} > 0\right]$ (Fig. 3(a)), the maximum positive $DK_{\psi s}$ and $FK_{\psi s}$ were placed at the same radial distance. Thus, it can be inferred that the flux convergence of $K_{\psi s}$ accounted for the inward radial movement of the maximum $K_{\psi s}$.

According to Eq. (2e), the flux divergence consists of horizontal flux divergence $\left[FK_{\psi s1}\right]$ and vertical flux divergence $\left[FK_{\psi s2}\right]$ of $K_{\psi s}$, and horizontal flux divergence of the geopotential $\left[FK_{\psi s3}\right]$, which are the first, second, and third terms on the right-hand side of Eq. (2e). The maximum flux convergence $[FK_{\psi s} > 0]$ is attributed mainly to the maximum horizontal flux divergence $[FK_{\psi s1} > 0]$ (Fig. 3(b)). Since the wind vectors can be expressed as

$$\boldsymbol{V} = \boldsymbol{V}_e + \boldsymbol{V}_{\psi s} + \boldsymbol{V}_{\psi a} + \boldsymbol{V}_{\chi s} + \boldsymbol{V}_{\chi a}, \tag{3}$$

$FK_{\psi s1}$ can be further separated as

$$\begin{aligned} FK_{\psi s1} =& \left(FK_{\psi s}\right)_{1e} + \left(FK_{\psi s}\right)_{1\psi s} + \left(FK_{\psi s}\right)_{1\psi a} \\ &+ \left(FK_{\psi s}\right)_{1\chi s} + \left(FK_{\psi s}\right)_{1\chi a}, \end{aligned} \tag{4}$$

where

$$\left(FK_{\psi s}\right)_{1e} = - < \nabla \cdot \left(\boldsymbol{V}_e \cdot \frac{\boldsymbol{V}_{\psi s}{}^2}{2}\right) >, \tag{4a}$$

$$\left(FK_{\psi s}\right)_{1\psi s} = - < \nabla \cdot \left(\boldsymbol{V}_{\psi s} \cdot \frac{\boldsymbol{V}_{\psi s}{}^2}{2}\right) >, \tag{4b}$$

$$\left(FK_{\psi s}\right)_{1\psi a} = - < \nabla \cdot \left(\boldsymbol{V}_{\psi a} \cdot \frac{\boldsymbol{V}_{\psi s}{}^2}{2}\right) >, \tag{4c}$$

$$\left(FK_{\psi s}\right)_{1\chi s} = - < \nabla \cdot \left(\boldsymbol{V}_{\chi s} \cdot \frac{\boldsymbol{V}_{\psi s}{}^2}{2}\right) >, \tag{4d}$$

$$\left(FK_{\psi s}\right)_{1\chi a} = - < \nabla \cdot \left(\boldsymbol{V}_{\chi a} \cdot \frac{\boldsymbol{V}_{\psi s}{}^2}{2}\right) > . \tag{4e}$$

Figure 3(c) shows that the horizontal flux convergence $[FK_{\psi s1} > 0]$ is attributable to the convergence of the flux of $K_{\psi s}$ by symmetric inward convergent radial flow $[(FK_{\psi s})_{1\chi s} > 0$; also see Fig. 5]. Therefore, the convergence of the flux of symmetric rotational kinetic energy through symmetric inward convergent radial flows is responsible for the inward radial movement of the maximum symmetric rotational kinetic energy.

At 17:00 UTC on July 17, the maximum $K_{\psi s}$ was collocated with the maximum $DK_{\psi s}$ (Fig. 4(a)), indicating that the maximum $K_{\psi s}$ was stationary. Analysis of the symmetric rotational kinetic energy budget revealed that the conversion from symmetric divergent kinetic energy to symmetric rotational kinetic energy $[(K_{\chi s}, K_{\psi s}) > 0]$ was the dominant factor in determining the maximum positive $DK_{\psi s}$. The horizontal advection $\left[(K_{\chi s}, K_{\psi s})_1\right]$, vertical advection $\left[(K_{\chi s}, K_{\psi s})_2\right]$ and the Coriolis force due to the Earth rotation $[(K_{\chi s}, K_{\psi s})_3]$ contribute toward $(K_{\chi s}, K_{\psi s})$; they are the first, second, and third terms on the right-hand side of (2b) while the separation calculation showed that $(K_{\chi s}, K_{\psi s})$ was determined by $(K_{\chi s}, K_{\psi s})_1$ (Fig. 4(b)). Substituting Eq. (3) into $(K_{\chi s}, K_{\psi s})_1$ yields

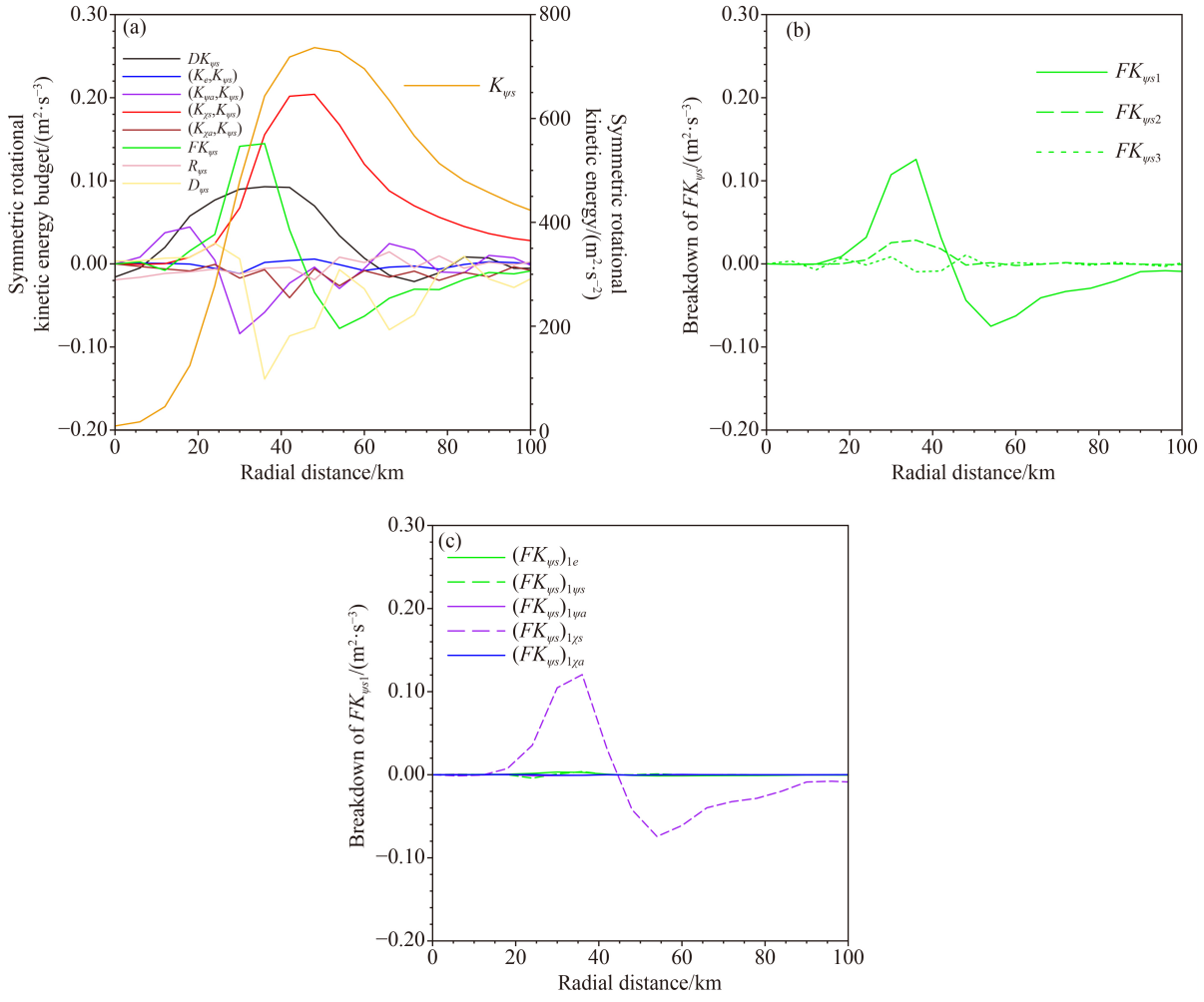

Fig. 3 Radial variations (km) of (a) symmetric rotational kinetic energy ($m^2 \cdot s^{-2}$) and its budget ($m^2 \cdot s^{-3}$) and (b)–(c) breakdowns of $FK_{\psi s}$ at 900 hPa at 00:00 UTC on July 17, 2014.

$$(K_{\chi s}, K_{\psi s})_1 = (K_{\chi s}, K_{\psi s})_{1e} + (K_{\chi s}, K_{\psi s})_{1\psi s} + (K_{\chi s}, K_{\psi s})_{1\psi a} + (K_{\chi s}, K_{\psi s})_{1\chi s} + (K_{\chi s}, K_{\psi s})_{1\chi a}, \tag{5}$$

$$(K_{\chi s}, K_{\psi s})_{1e} = - < \boldsymbol{V}_{\psi s} \cdot (\boldsymbol{V}_e \cdot \nabla)\boldsymbol{V}_{\chi s} >, \tag{5a}$$

$$(K_{\chi s}, K_{\psi s})_{1\psi s} = - < \boldsymbol{V}_{\psi s} \cdot (\boldsymbol{V}_{\psi s} \cdot \nabla)\boldsymbol{V}_{\chi s} >, \tag{5b}$$

$$(K_{\chi s}, K_{\psi s})_{1\psi a} = - < \boldsymbol{V}_{\psi s} \cdot (\boldsymbol{V}_{\psi a} \cdot \nabla)\boldsymbol{V}_{\chi s} >, \tag{5c}$$

$$(K_{\chi s}, K_{\psi s})_{1\chi s} = - < \boldsymbol{V}_{\psi s} \cdot (\boldsymbol{V}_{\chi s} \cdot \nabla)\boldsymbol{V}_{\chi s} >, \tag{5d}$$

$$(K_{\chi s}, K_{\psi s})_{1\chi a} = - < \boldsymbol{V}_{\psi s} \cdot (\boldsymbol{V}_{\chi a} \cdot \nabla)\boldsymbol{V}_{\chi s} > . \tag{5e}$$

The partitioning computation indicated that positive $\left(K_{\chi s}, K_{\psi s}\right)_1$ was mainly associated with positive horizontal advection via symmetric rotational circulations [$(K_{\chi s}, K_{\psi s})_{1\psi s} > 0$] (Fig. 4(c)). In cylindrical coordinates, $(K_{\chi s}, K_{\psi s})_{1\psi s}$ can be written as

$$(K_{\chi s}, K_{\psi s})_{1\psi s} = (K_{\chi s}, K_{\psi s})_{1\psi s,A} + (K_{\chi s}, K_{\psi s})_{1\psi s,B} + (K_{\chi s}, K_{\psi s})_{1\psi s,C} + (K_{\chi s}, K_{\psi s})_{1\psi s,D}, \tag{6}$$

$$(K_{\chi s}, K_{\psi s})_{1\psi s,A} = - < v_{\psi sr} \cdot v_{\psi sr} \frac{\partial v_{\chi sr}}{\partial r} >, \tag{6a}$$

$$(K_{\chi s}, K_{\psi s})_{1\psi s,B} = - < v_{\psi sr} \cdot v_{\psi s\theta} \frac{\partial v_{\chi s\theta}}{\partial r} >, \tag{6b}$$

$$(K_{\chi s}, K_{\psi s})_{1\psi s,C} = - < \frac{v_{\psi s\theta}}{r} v_{\psi s\theta} v_{\chi sr} >, \tag{6c}$$

$$(K_{\chi s}, K_{\psi s})_{1\psi s,D} = < \frac{v_{\psi s\theta}}{r} v_{\psi sr} v_{\chi s\theta} > . \tag{6d}$$

The Coriolis force due to typhoon rotation $\left[(K_{\chi s}, K_{\psi s})_{1\psi s,C} > 0\right]$ determines the positive $(K_{\chi s}, K_{\psi s})_{1\psi s}$ (Fig. 4(d)). The tangential component of the symmetric rotational wind $\left[v_{\psi s\theta}\right]$ is cyclonic within a radial distance of 0–100 km (Fig. 5). $v_{\psi s\theta}$ increases as the radial distance increases from 0 to 30 km, whereas it decreases as the radial distance continues to increase from 30 to 100 km. The radial component of the symmetric divergent wind $\left[v_{\chi sr}\right]$

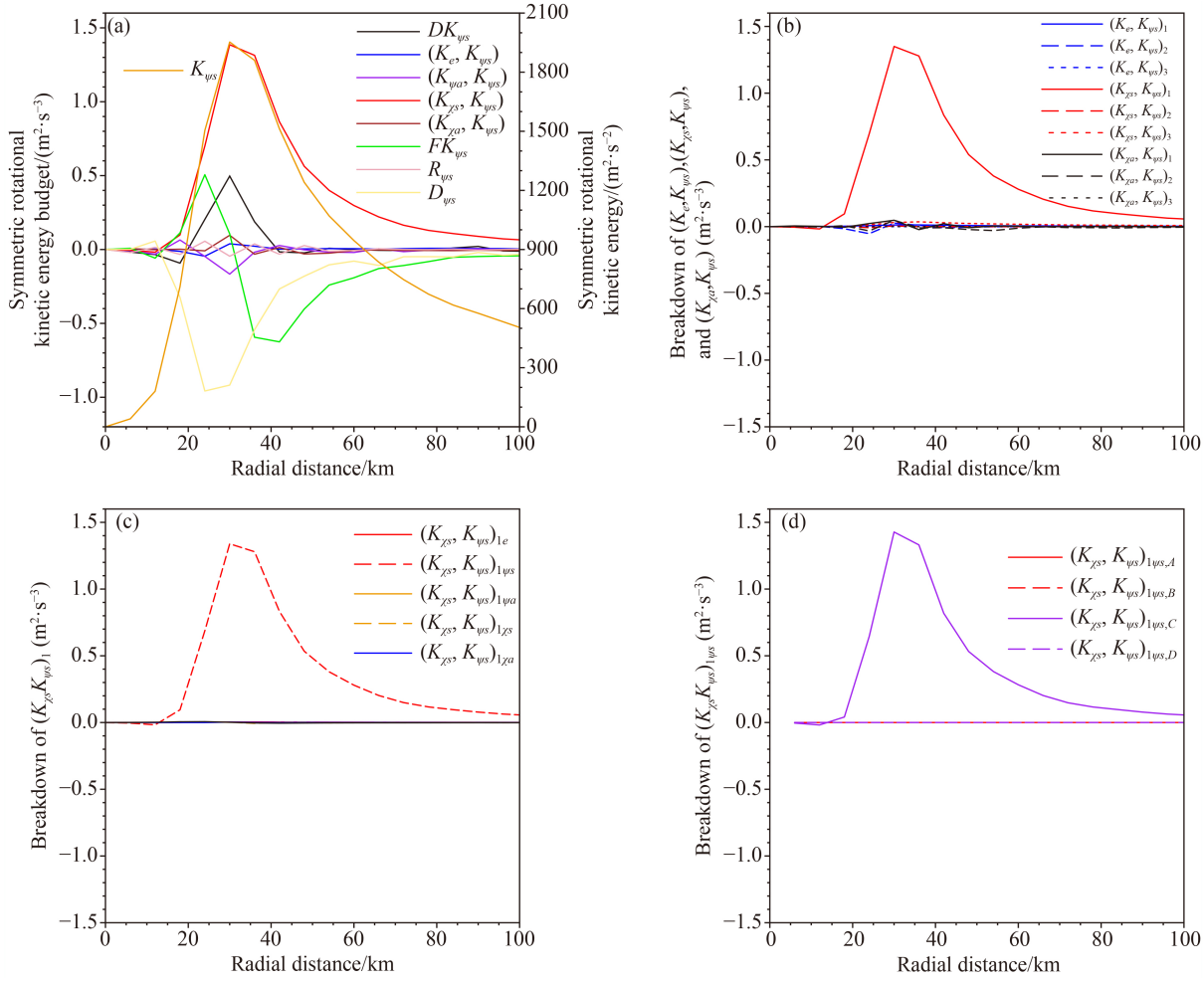

Fig. 4 Radial variations (km) of (a) symmetric rotational kinetic energy ($m^2 \cdot s^{-2}$) and its budget ($m^2 \cdot s^{-3}$) and (b)–(d) breakdowns of $(K_{\chi s}, K_{\psi s})$ at 900 hPa at 17:00 UTC on July 17, 2014.

is inward within a radial distance of 0–100 km. The magnitude of $v_{\chi sr}$ increases as the radial distance increases from 0 to 35 km whereas it decreases as the radial distance increases from 35 to 100 km. It can be observed that the negative correlation between $v_{\psi s\theta}$ and $v_{\chi sr}$ led to the dominance of $(K_{\chi s}, K_{\psi s})$ in the maximum positive tendency of $K_{\psi s}$, which caused the maximum $K_{\psi s}$ to be stationary.

To examine which physical process compensated for the loss of $K_{\chi s}$ that was converted to $K_{\psi s}$, the budget of symmetric divergent kinetic energy was calculated. The budget can be expressed as

$$DK_{\chi s} = (K_e, K_{\chi s}) - (K_{\chi s}, K_{\psi s}) - (K_{\chi s}, K_{\psi a}) + (K_{\chi a}, K_{\chi s}) + (P, K_{\chi s}) + FK_{\chi s} + D_{\chi s} + R_{\chi s}, \quad (7)$$

$$(K_e, K_{\chi s}) = - < \boldsymbol{V}_{\chi s} \cdot (\boldsymbol{V} \cdot \nabla) \boldsymbol{V}_{\chi s} > - < \omega \frac{\partial}{\partial p} \boldsymbol{V}_{\chi s} \cdot \boldsymbol{V}_{\chi a} > - < f(\boldsymbol{k} \times \boldsymbol{V}_{\chi s}) \cdot \boldsymbol{V}_{\chi a} >, \quad (7a)$$

$$(K_{\chi s}, K_{\psi a}) = - < \boldsymbol{V}_{\psi a} \cdot (\boldsymbol{V} \cdot \nabla) \boldsymbol{V}_{\chi s} > - < \omega \frac{\partial}{\partial p} \boldsymbol{V}_{\chi s} \cdot \boldsymbol{V}_{\psi a} > - < f(\boldsymbol{k} \times \boldsymbol{V}_{\chi s}) \cdot \boldsymbol{V}_{\psi a} >, \quad (7b)$$

$$(K_{\chi a}, K_{\chi s}) = - < (\boldsymbol{V} \cdot \nabla \boldsymbol{V}_{\chi a}) \cdot \boldsymbol{V}_{\chi s} > - < \omega \frac{\partial}{\partial p} \boldsymbol{V}_{\chi a} \cdot \boldsymbol{V}_{\chi s} > - < f(\boldsymbol{k} \times \boldsymbol{V}_{\chi a}) \cdot \boldsymbol{V}_{\chi s} >, \quad (7c)$$

$$FK_{\chi s} = - < \nabla \cdot \left[\boldsymbol{V} \left(\frac{\boldsymbol{V}_{\chi s}^2}{2} \right) \right] > - < \frac{\partial}{\partial p} \left[\omega \left(\frac{\boldsymbol{V}_{\chi s}^2}{2} \right) \right] > - < \nabla \cdot \left[\boldsymbol{V} (\boldsymbol{V}_{\psi s} \cdot \boldsymbol{V}_{\chi s}) \right] > - < \nabla \cdot \left[\boldsymbol{V} (\boldsymbol{V}_{\psi a} \cdot \boldsymbol{V}_{\chi s}) \right] > - < \frac{\partial}{\partial p} \left[\omega (\boldsymbol{V}_{\psi s} \cdot \boldsymbol{V}_{\chi s}) \right] > - < \frac{\partial}{\partial p} \left[\omega (\boldsymbol{V}_{\psi a} \cdot \boldsymbol{V}_{\chi s}) \right] >, \quad (7d)$$

$$D_{\chi s} = \boldsymbol{V}_{\chi s} \cdot \boldsymbol{F}, \quad (7e)$$

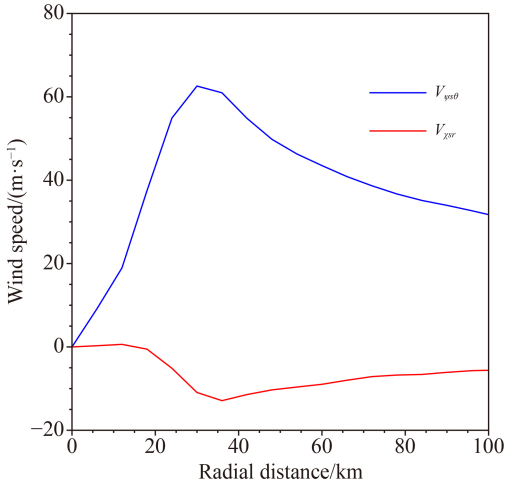

Fig. 5 Radial variations (km) of tangential component of symmetric rotational wind (blue) and radial component of symmetric divergent wind (red) at 900 hPa at 17:00 UTC on July 17, 2014. The unit of wind speed is m·s^{-1}.

$$R_{\chi s} = - < \boldsymbol{V}_{\chi s} \cdot \frac{\partial}{\partial t}\boldsymbol{V}_e > - < \boldsymbol{V}_{\chi s} \cdot \frac{\partial}{\partial t}\boldsymbol{V}_{\psi s} >, \tag{7f}$$

$$\left(P, K_{\chi s}\right) = - < \boldsymbol{V}_{\chi s} \cdot \nabla \varnothing > . \tag{7g}$$

The definitions and physical meanings of the symbols in Eq. (7) are listed in Table 2.

The calculation of the budget of symmetric divergent kinetic energy shows that the conversion from symmetric divergent kinetic energy to symmetric rotational kinetic energy was balanced by the conversion from potential energy to symmetric divergent kinetic energy through the work done by symmetric divergent circulations against the geopotential gradient (Fig. 6(a)). $\left(P, K_{\chi s}\right)$ can be broken down as follows:

$$\left(P, K_{\chi s}\right) = \left(P, K_{\chi s}\right)_1 + \left(P, K_{\chi s}\right)_2, \tag{8}$$

$$\left(P, K_{\chi s}\right)_1 = - < v_{\chi sr} \frac{\partial \varnothing}{\partial r} >, \tag{8a}$$

$$\left(P, k_{\chi s}\right)_2 = - < v_{\chi s\theta} \frac{1}{r} \frac{\partial \varnothing}{\partial \theta} > . \tag{8b}$$

The breakdown calculation reveals that the potential energy was converted to symmetric divergent kinetic energy through the work done by symmetric inward convergent radial flows against the geopotential gradient (Fig. 6(b)).

At 12:00 UTC on July 18, dissipation ($D_{\psi s}$), conversion of symmetric rotational kinetic energy to asymmetric rotational kinetic energy $[\left(K_{\psi a}, K_{\psi s}\right) < 0]$, and flux divergence of symmetric rotational kinetic energy ($FK_{\psi s} < 0$) contributed to the decrease in maximum $K_{\psi s}$, although the three factors were largely offset by the conversion of symmetric divergent kinetic energy to symmetric rotational kinetic energy $\left[\left(K_{\chi s}, K_{\psi s}\right) > 0\right]$ (Fig. 7). Considering the three terms representing these factors, the magnitude of dissipation is much larger than those of the other two factors. Thus, dissipation is inferred to be responsible for the decrease in the maximum $K_{\psi s}$ as well as the outward movement of the maximum $K_{\psi s}$.

Table 2 Definitions and physical meanings of symbols used in Equations

Symbol	Definition and physical meanings
$K_{\psi s}$	Symmetric rotational kinetic energy
$K_{\psi a}$	Asymmetric rotational kinetic energy
$K_{\chi s}$	Symmetric divergent kinetic energy
$K_{\chi a}$	Asymmetric divergent kinetic energy
$DK_{\psi s}$	Tendency of symmetric rotational kinetic energy
$DK_{\chi s}$	Tendency of symmetric divergent kinetic energy
$\left(K_e, K_{\psi s}\right)$	Conversion between environmental kinetic energy and symmetric rotational kinetic energy
$\left(K_{\psi a}, K_{\psi s}\right)$	Conversion between asymmetric rotational kinetic energy and symmetric rotational kinetic energy
$\left(K_{\chi s}, K_{\psi s}\right)$	Conversion between symmetric divergent kinetic energy and symmetric rotational kinetic energy
$\left(K_{\chi a}, K_{\psi s}\right)$	Conversion between asymmetric divergent kinetic energy and symmetric rotational kinetic energy
$\left(K_e, K_{\chi s}\right)$	Conversion between environmental kinetic energy and symmetric divergent kinetic energy
$\left(K_{\chi s}, K_{\psi a}\right)$	Conversion between symmetric divergent kinetic energy and asymmetric rotational kinetic energy
$\left(K_{\chi a}, K_{\chi s}\right)$	Conversion between asymmetric divergent kinetic energy and symmetric divergent kinetic energy
$\left(P, K_{\chi s}\right)$	Conversion between potential energy and symmetric divergent kinetic energy
$FK_{\psi s}$	Convergence of flux of symmetric rotational kinetic energy
$FK_{\chi s}$	Convergence of flux of symmetric divergent kinetic energy
$D_{\psi s}$	Dissipation of symmetric rotational kinetic energy
$D_{\chi s}$	Dissipation of symmetric divergent kinetic energy
$R_{\psi s}$	Product of symmetric rotational wind and tendencies of environmental wind and symmetric divergent wind
$R_{\chi s}$	Product of symmetric divergent wind and tendencies of environmental wind and symmetric rotational wind
$\boldsymbol{V}$	Horizontal wind
$\boldsymbol{V}_e$	Environmental wind
$\boldsymbol{V}_{\psi s}$	Symmetric rotational wind
$\boldsymbol{V}_{\psi a}$	Asymmetric rotational wind
$\boldsymbol{V}_{\chi s}$	Symmetric divergent wind
$\boldsymbol{V}_{\chi a}$	Asymmetric divergent wind
ω	Vertical velocity in pressure coordinates
$\boldsymbol{k}$	Unit vector in vertical direction
f	Coriolis parameter corresponding to the Earth's rotation
$\varnothing$	Geopotential
∇	Horizontal differential operator
$\boldsymbol{F}$	Friction force

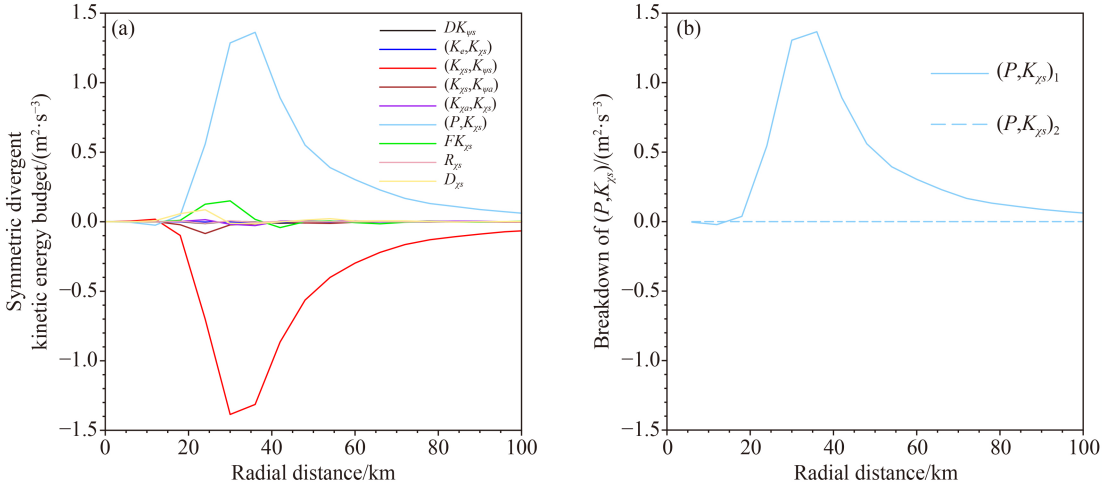

Fig. 6 Radial variation (km) of (a) symmetric divergent kinetic energy budget ($m^2 \cdot s^{-3}$) and (b) breakdown of $\left(P, K_{\psi s}\right)$ at 900 hPa at 17:00 UTC on July 17, 2014.

4 Conclusions

In this study, Typhoon Rammasun, which occurred in 2014, was simulated using the WRF model, and validated simulation data for the lower troposphere were used to study the physical processes responsible for the movement of the maximum winds. The maximum wind and its movement were respectively measured by the maximum symmetric rotational kinetic energy and its radial movement. Before RI, the radial distance of the maximum symmetric rotational kinetic energy decreased with time, with barely any change during RI. After RI, the radial distance increased with time. A comparison of these radial distances, and an analysis of the budget of the symmetric rotational kinetic energy was carried out to examine the physical processes that account for the radial movement of the maximum wind of the tropical cyclone.

Budget analyses of symmetric rotational kinetic energy ($K_{\psi s}$) revealed that the maximum $K_{\psi s}$ tendency in the lower troposphere was mainly determined by the flux convergence of $K_{\psi s}$ [$FK_{\psi s}$], conversion from symmetric divergent kinetic energy ($K_{\chi s}$) to symmetric rotational kinetic energy $\left[\left(K_{\chi s}, K_{\psi s}\right) > 0\right]$, and dissipation ($DK_{\psi s} < 0$). Partition analyses showed that $FK_{\psi s}$ was dominated by the radial flux convergence of the symmetric rotational kinetic energy $\left[-\frac{1}{r}\frac{\partial}{\partial r}\left(rv_{\chi sr}K_{\psi s}\right)\right]$, which was mainly controlled by the radial derivative of $K_{\psi s}$. $\left(K_{\chi s}, K_{\psi s}\right)$ was controlled by the collocation of $v_{\chi sr}$ and $K_{\psi s}$ $\left(-\frac{2}{r}v_{\chi sr}K_{\psi s}\right)$. $FK_{\psi s}$ reaches its maximum at the radius corresponding to the maximum $K_{\psi s}$ while maximum $FK_{\psi s}$ converges within the radius of the maximum $K_{\psi s}$. Thus, convergent $FK_{\psi s}$ accounts for the inward movement of the maximum $K_{\psi s}$. The maximum conversion from $K_{\chi s}$ to $K_{\psi s}$ occurs at the maximum $K_{\psi s}$, indicating that maximum $K_{\psi s}$ is stationary. The maximum negative $K_{\psi s}$ tendency associated with the dissipation explains the outward movement of maximum $K_{\psi s}$.

The physical processes associated with the radial movement of maximum symmetric rotational kinetic energy are shown in Fig. 8. Before RI, the maximum flux convergence of the symmetric rotational kinetic energy is larger than the conversion, leading to the inward movement of the maximum $K_{\psi s}$. During RI, symmetric cyclonic circulation develops significantly, and the conversion dominates $K_{\psi s}$ tendency, causing the maximum symmetric rotational kinetic energy to be stationary. When Rammasun made landfall, the terrain-induced friction dissipation overcame the conversion, resulting in the outward movement of maximum $K_{\psi s}$, thus ending the RI.

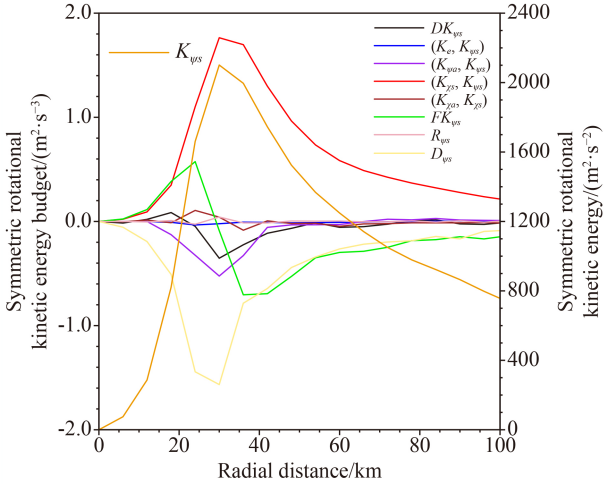

Fig. 7 Radial variations (km) of symmetric rotational kinetic energy ($m^2 \cdot s^{-2}$) and its budget ($m^2 \cdot s^{-3}$) at 900 hPa at 12:00 UTC on July 18, 2014.

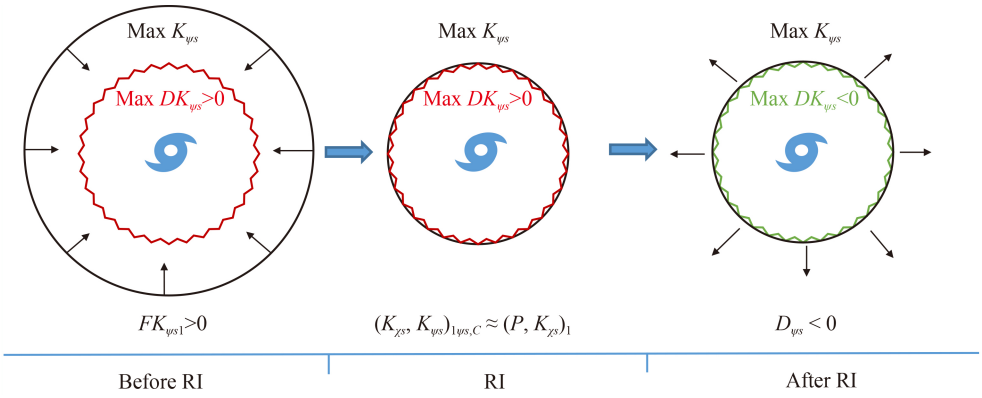

Fig. 8 Schematic diagram that highlights physical processes responsible for radial movement of maximum symmetric rotational kinetic energy ($K_{\psi s}$) associated with maximum winds during different stages of development of Typhoon Rammasun (2014). $K_{\psi s}$ is symmetric rotational kinetic energy; $DK_{\psi s}$ is the tendency of $K_{\psi s}$; $FK_{\psi s1}$ is the horizontal flux convergence of $K_{\psi s}$; $(K_{\chi s}, K_{\psi s})_{1\psi s,C}$ is conversion between symmetric divergent kinetic energy ($K_{\chi s}$) and $K_{\psi s}$ through interaction between symmetric cyclonic tangential wind and symmetric inward radial wind; $(P, K_{\chi s})$ is the transfer from potential energy (P) to $K_{\chi s}$ through work done by symmetric inward radial flow against geopotential gradient; $D_{\psi s}$ is the dissipation.

Caution should be exercised when applying the results of this study because only the kinetic energy budgets were analyzed. As discussed in the Introduction, previous studies have used different methods to examine the dominant processes responsible for the movement of maximum wind. We plan to undertake a study comparing the use of the kinetic energy budget—as done in this study—with other methods employed in previous studies in the future, to generalize the results from all studies. Previous studies have shown that in addition to dynamic processes, diabatic processes, such as surface enthalpy flux associated with sea surface temperature (e.g., Sun et al., 2014) have important impacts on the inner-core size of tropical cyclones. The important effects of such processes on the radial movement of maximum wind will be examined in our future studies—within the energy framework—with the surface enthalpy flux included in the budget of available potential energy.

Acknowledgments The authors thank the Training Center of Atmospheric Sciences of Zhejiang University and the two anonymous reviewers for their constructive comments and suggestions. We also thank Huiyan Xu for deriving kinetic energy equations, Liguang Wu and Huarui Zhao for providing the MWT filter codes, Xinyong Shen for improving the simulation of Typhoon Rammasun, and Liangliang Li and Chi Zhang for valuable discussions. This study was supported by the National Natural Science Foundation of China (Grant No. 41930967).

References

Bougeault P, Lacarrere P (1989). Parameterization of orography-induced turbulence in a mesobeta-scale model. Mon Weather Rev, 117(8): 1872–1890

Dudhia J (1989). Numerical study of convection observed during the winter monsoon experiment using a mesoscale two-dimensional model. J Atmos Sci, 46(20): 3077–3107

Ek M B, Mitchell K E, Lin Y, Rogers E, Grunmann P, Koren V, Gayno G, Tarpley J D (2003). Implementation of Noah land surface model advances in the National Centers for Environmental Prediction operational mesoscale Eta model. J Geophys Res, 108(D22): 8851

Hong S Y, Lim J O J (2006). The WRF Single-Moment 6-Class Microphysics Scheme (WSM6). J Korean Meteor Soc, 42(2): 129–151

Kain J S (2004). The Kain-Fritsch convective parameterization: an update. J Appl Meteorol, 43(1): 170–181

Kalnay E, Kanamitsu M, Kistler R, Collins W, Deaven D, Gandin L, Iredell M, Saha S, White G, Woollen J, Zhu Y, Chelliah M, Ebisuzaki W, Higgins W, Janowiak J, Mo K C, Ropelewski C, Wang J, Leetmaa A, Reynolds R, Jenne R, Joseph D (1996). The NCEP/NCAR reanalysis 40-year project. Bull Amer Meteo Soc, 77(3): 437–471

Kieu C Q (2012). An investigation into the contraction of the hurricane radius of maximum wind. Meteorol Atmos Phys, 115(1–2): 47–56

Kurihara Y, Bender M A, Ross R J (1993). An initialization scheme of hurricane models by vortex specification. Mon Weather Rev, 121(7): 2030–2045

Kurihara Y, Bender M A, Tuleya R E, Ross R J (1995). Improvements in the GFDL Hurricane Prediction System. Mon Weather Rev, 123(9): 2791–2801

Li A, Zhang L, Zang Z, Zhang Y (2012). Computation of stream function and velocity potential in a limited area and its application to typhoon. J Meteorol Sci, 32(1): 1−8 (in Chinese)

Li Y, Wang Y, Lin Y (2019). Revisiting the dynamics of eyewall contraction of tropical cyclones. J Atmos Sci, 76(10): 3229–3245

Li Y, Wang Y, Lin Y, Wang X (2021). Why does rapid contraction of the radius of maximum wind precede rapid intensification in tropical cyclones? J Atmos Sci, 78(11): 3441–3453

Liang X S, Anderson D G M (2007). Multiscale window transform. Multiscale Model Simul, 6(2): 437–467

Mlawer E J, Taubman S J, Brown P D, Iacono M J, Clough S A (1997). Radiative transfer for inhomogeneous atmospheres: RRTM, a validated correlated-k model for the longwave. J Geophys Res,

102(D14): 16663–16682

Moon I J, Ginis I, Hara T, Thomas B (2007). A physics-based parameterization of air–sea momentum flux at high wind speeds and its impact on hurricane intensity predictions. Mon Weather Rev, 135(8): 2869–2878

Qin N, Wu L (2021). Possible environmental inflence on eyewall expansion during the rapid intensification of hurricane Helene (2006). Front Earth Sci, 9(7): 715012

Qin N, Zhang D L, Li Y (2016). A statistical analysis of steady eyewall sides associated with rapidly intensifying hurricanes. Weather Forecast, 31(3): 737–742

Skamarock W C, Klemp J B, Dudhia J, Gill D O, Liu Z, Berner J, Wang W, Powers J G, Duda M G, Barker D M, Huang X (2019), A description of the advanced research WRF Model Version 4, NCAR Tech, Note NCAR/TN-556+STR

Stern D P, Vigh J L, Nolan D S, Zhang F (2015). Revisiting the relationship between eyewall contraction and intensification. J Atmos Sci, 72(4): 1283–1306

Sun Y, Zhong Z, Yi L, Ha Y, Sun Y (2014). The opposite effects of inner and outer sea surface temperature on tropical cyclone intensity. J Geophys Res Atmos, 119(5): 2193–2208

Willoughby H E, Clos J A, Shoreibah M G (1982). Concentric eye walls, secondary wind maxima, and the evolution of the hurricane vortex. J Atmos Sci, 39(2): 395–411

Zhao H, Wu L, Liang X (2015). Preliminary application of the MWT method to separate tropical cyclone circulation. Adv Meteor Sci Technol, 5(6): 31−36 (in Chinese)